Preprints.org

Experimental and Simulation Studies on the Mn Oxidation State Evolution of a Li2O-MnOx-CaO-SiO2 Slag Analogue

Sven Hampel , Iyad Alabd Alhafez , Alena Schnickmann , Sophie Wunderlich , Haojie Li ,

Michael Fischlschweiger , Thomas Schirmer , Nina Merkert , Ursula E. A. Fittschen [*]

Article

Experimental and simulation studies on the Mn oxidation state evolution of a Li_2O-MnO_x-CaO-SiO_2 slag analogue

Sven Hampel [1,†] (ID), Iyad Alabd Alhafez [2], Alena Schnickmann [3], Sophie Wunderlich [1], Haojie Li [4], Michael Fischlschweiger [4] (ID), Thomas Schirmer [3] (ID), Nina Merkert [2] (ID) and Ursula E. A. Fittschen [1,*]

[1] Clausthal University of Technology, Institute of Inorganic and Analytical Chemistry, Arnold-Sommerfeld-Str. 4, 38678 Clausthal-Zellerfeld, Germany; sven.hampel@tu-clausthal.de (S.H.); sophie.wunderlich@tu-clausthal.de (S.W.)
[2] Clausthal University of Technology, Institute of Applied Mechanics, Arnold-Sommerfeld-Str. 6, 38678 Clausthal-Zellerfeld, Germany; iyad.alabd.alhafez@tu-clausthal.de (I.A.A.); nina.merkert@tu-clausthal.de (N.M.)
[3] Clausthal University of Technology, Institute of Repository Research, Adolph-Roemer-Str. 2A, 38678 Clausthal-Zellerfeld, Germany; alena.schnickmann@tu-clausthal.de (A.S.); thomas.schirmer@tu-clausthal.de (T.S.)
[4] Clausthal University of Technology, Institute of Energy Process Engineering and Fuel Technology, Agricolastr. 4, 38678 Clausthal-Zellerfeld, Germany; haojie.li@tu-clausthal.de (H.L.); michael.fischlschweiger@tu-clausthal.de (M.F.)
[*] Correspondence: ursula.fittschen@tu-clausthal.de; Tel.: +49-5323-72-2205
[†] Current address: Centre for X-ray and Nano Science, Deutsches Elektronen-Synchrotron, Notkestr. 85, 22607 Hamburg, Germany

Abstract: A better understanding of high temperature processes in slags contributes to facilitate knowledge based design of the solidified product. Here, a slag analogue with a nominal composition of 17 wt% $LiMnO_2$ and 83 wt% Ca_2SiO_4 was synthesized encountering fairly high cooling rates. The Mn species from 1223 K to 1773 K was simulated using a thermodynamic model assuming a homogeneous melt. The micro-composition including the Mn species of the solidified slag was determined experimentally and was used as basis for molecular dynamics (MD) simulation. The MD simulation provides information on structure and viscosity at high temperatures, otherwise difficult to access. These parameters significantly influence oxidation state of redox-active elements and the solidified product. The micro-composition analyzed by electron probe micro analysis (EPMA) and synchrotron based micro-X-ray fluorescence (micro-XRF) showed that Mn-rich and Ca-Si-rich phases are separated. While the Mn-O phases did not contain noticeable Ca, the Ca_2SiO_4 phase had incorporated 0.6 wt% of Mn. The slag solidified into round shaped and droplet shaped grains of a Li-Mn-oxide, some Mn_3O_4 and Ca_2SiO_4. The powder X-ray diffraction (PXRD) confirmed the formation of larnite, the identity of the Li-Mn-oxide however remained inconclusive. The Mn oxidation state (OS) was identified using synchrotron based micro-X-ray absorption near edge spectroscopy (micro-XANES). The Mn-O grains, matched well with Li-Mn-oxides and a Mn OS: +3 *e.g.* $LiMn^{3+}O_2$. Small areas matching Hausmannite ($Mn^{2+}Mn_2^{3+}O_4$) were also identified. The OS of Mn in the silicate phase could not be identified. For comparison a slowly cooled slag analogue with similar composition however higher Si content, was also subjected to micro-XANES. The slowly cooled slag formed long Mn-rich needles in a matrix of large calcium silicate crystals. The Mn-rich crystals matched well with the XANES spectrum of a Mn^{3+} Li-oxide like $LiMn^{3+}O_2$. At the rim of the needles the Mn-spectra matched well the Hausmannite ($Mn^{2+}Mn_2^{3+}O_4$) reference. In the silicate phases Mn had a OS: +2, unambiguously. The melt structure at different temperatures of two compositions *i.e.* $LiMn^{3+}O_2$ and Ca_2SiO_4 was simulated using molecular dynamics (MD). They serve as model compositions assuming a heterogeneous melt. The results show significant different degrees of polymerization and viscosity. Information from MD simulations can support the identification of potentially different oxygen permeability and with that prediction of oxidation states. The bulk composition was identified by inductively coupled plasma optical emission spectrometry (ICP-OES), bulk structure by PXRD and bulk species by lab-XANES. The synchrotron micro analysis including micro-XRD were performed at the microfocus beamline I18 at the Diamond Light Source. Pure reference compounds were prepared and characterized with the same multi-modal approach.

Keywords: engineered artificial minerals (EnAM); lithium battery recycling; XANES; EPMA; molecular dynamic simulation

1. Introduction

Tailoring metallurgical slags to facilitate an optimal production of a high quality metallic product has been a topic of research and development for a long time [1,2]. In recent years, interest rose to tailor slags to produce recoverable compounds which incorporate critical elements. Materials and elements are considered critical, when they are highly important for the economy and their supply security is easily jeopardized. The recoverable synthesized slag compounds are sometimes referred to as engineered artificial minerals (EnAM). The recovery of lithium from Li-ion battery recycling slags in form of a scavenger compound has been studied by *e.g.* Elvert *et al.* [3]. The early crystallizing $LiAlO_2$ was identified as as promising EnAM and it was shown that it can be separated from gehlenite $Ca_2Al[AlSiO_7]$ using froth flotation obtaining a recovery of 88% [4]. Wittkowski *et al.* [5] has shown that with rising concentrations of Mn (*approx.* 7%) the yield of $LiAlO_2$ decreases and Li is incorporated into Mn-Al-oxide spinel solid solutions. Schnickmann *et al.* suggested Li-Mn-oxides as alternative EnAM in the Li_2O-SiO_2-CaO-MnO_n-(MgO)-(Al_2O_3) system. They found that if Al is excluded from the system Li is incorporated nearly completely in early crystallizing $LiMnO_2$ [6]. The oxidation state of Mn in these artificial slags, produced in ambient air was determined to be mainly +3. From thermodynamic calculations by Longo *et al.* [7] it can be deducted that Mn in an oxidation state +4 in form of Li_2MnO_3 is even stabilized in the presence of Al, which emphasizes the importance of understanding how the Mn oxidation state is controlled.

With respect to the studied system it can be concluded that besides Mn none of the metal ions may act as reducer or oxidizer, leaving gases like O_2 and CO as redox-reactive species. The concentration of O_2 in the melt will depend on the temperature, with high temperatures in general supporting the gas phase and its permeability. Mainly, two processes have been discussed influencing the permeability of O_2 in slags, which are the viscosity [2,8] and reactive dissolution of oxygen by reacting with reduced metal species like Fe^{2+} [9]. A fluid melt enables oxygen diffusivity, while high temperatures favour higher O_2 concentrations in the gas phase. The viscosity depends on the composition of the melt and can be estimated with the concepts of identifying the relation of network former and network modifier. Silicon and Al are considered network former while Li, Ca and Mn are considered network modifier [2]. For the Li-ion recycling slag system, the SiO_2 fraction is *approx.* 20 mol% a degree of polymerization being Q = 2.7 (4 highest degrees and 0 lowest degrees of polymerization) was calculated. The Q value is obtained from Q = 4-NBO/T and can be considered as the average of the Q^n structural units.

Making use of thermodynamic data oxygen equilibrium between the liquid and gas phase can be described. The Calculation of Phase Diagrams (Calphad) method [10] combines different experimental data, such as thermal, caloric properties and phase diagram information, as well as ab initio data to develop thermodynamic databases for predicting materials' phase behaviour. This is of particular importance for, *e.g.*, understanding solidification and phase formation. Nowadays, this method is also widely applied to Li-containing oxide material systems to predict respective phase diagrams and solidification [11–16]. The commercial databases FToxide and FactPS [13] can be used to understand and predict heterogeneous phase behavior considering gas, liquid, and solid phases and composition during equilibrium solidification. It can be applied to understand the temperature dependent variation of manganese valence in the liquid slag in relation to O_2 dissolved in the melt.

The viscosity of a certain composition present in an in-homogeneous melt, in-homogeneous *e.g.* because of liquid-liquid and solid liquid phase separation, can be derived describing the compounds on an atomistic level using molecular dynamic simulations. This has the advantage, that the viscosity at any temperature from above to below the liquidus and even at very high temperatures is accessible. The degree of polymerization can also be determined. Molecular modelling allows to investigate the elemental interaction of various elements in a molten state and obtain the RDFs and mean square displacements (MSD). MD simulations are based on Newton's equations of motion, which are solved by so-called integrators. The forces are calculated from interatomic interaction potentials. Further essential components of an MD simulation are the choice of the time step and the definition of the boundary conditions, *e.g.*, by thermostats or barostats. In a post-processing step, the element coordination,

viscosity and network formation in the melt can be determined. The influence of parameters like temperature or concentration gradients can be studied to achieve an efficient slag design, this mostly with respect to an optimal metal product. A recent review is found by Zhou *et al.* [17]. MD simulations have been frequently used to obtain the short-range ordered structure of molten slags and the melt's kinetic characteristics [18,19]. MD research had focused on the analysis of different slag systems including silicate slags [20], Al slags [21] and aluminosilicate slags [22,23]. With respect to the lithium EnAM, lithium aluminates have been studied with MD simulations and experimentally. Individual diffusivities depend on the Li:Al ratio and strongly decrease viscosity [24]. The effect of Mn has been less explored. The network breaking properties of MnO in Al_2O_3-SiO_2-CaO-MnO slags were described using MD simulation [19].

The composition of the melt is fundamental for the macroscopic properties. A major challenge for obtaining the accurate composition when the Mn species is formed, are the uncertainties on local gradients. The local composition is affected by phase separations, these are solid-liquid (SL) separations but also liquid-liquid (LL) and gas-liquid (GL) separations. The local composition may encounter sharp boundaries if LL-phase separation occurs and compositional gradients while the solidification proceeds. These gradients can be described incrementally from systems with reduced complexity. This has been done for $LiAlO_2$ and for the thermodynamically predicted compounds sharing its precipitation zone which are $LiAl_5O_8$ spinel and Li_5AlO_4 [24] and a recent review paper describes this approach [25]. In this work the system Li_2O-MnO_x-SiO_2-CaO is studied. The slag analogue, which had encountered fairly steep cooling rates during its genesis, showed a separation of Si-Ca and Mn-rich phases with the Si-Ca phases containing minor amounts of Mn. The shape of the separated phase is round and in case of the Mn-rich compounds droplet shaped. The Mn species of the micro-compounds was characterized using micro-XANES strongly supporting the Mn-rich compounds being Li-Mn^{3+} oxides. As the concentration of Mn in the Si-Ca phase was very low, a slowly cooled slag analogue of the same system was also studied. Two compounds representing the Li-Mn-O and the Ca-Si-O phases were studied separately with MD simulations at high temperatures and the individual viscosity was determined. Future simulations will need to included minor elements present in the micro-compounds, to get closer to the description of the real system.

2. Materials and Methods

2.1. Molecular Dynamic Simulations.

All the molecular dynamics simulations are performed with the open-source LAMMPS code [26]. In all simulations time steps of 1 fs were chosen with periodic boundary conditions. In the slag analogue mostly calcium silicate Ca_2SiO_4 and a lithium manganate(III) were present hence larnite and $LiMnO_2$ were studied by charged particles interactions. They are described by the long range Coulomb and the short range Buckingham potential (equation 1):

$$V_{ij} = \frac{1}{4\pi\varepsilon_0} \frac{q_i q_j}{r_{ij}} + \left[A_{ij} \exp\left(\frac{-r_{ij}}{\rho_{ij}} \right) - \frac{C_{ij}}{r_{ij}^6} \right] \qquad (1)$$

Here i and j denote an interacting pair of two ions among the present elements separated by a distance r_{ij}, ε_0 stands for the dielectric constant. The Buckingham potential parameters are taken from Cormack and Du [27] as well as Sayle *et al.* [28] and are listed in Table 1.

Table 1. Interatomic potential parameters used in the atomistic simulations of Li-Mn-O system (top) and Ca-Si-O system (bottom)

Interaction	A (eV)	ρ(Å)	C (eV Å^6)	charge
$Li^+ - Li^+$	270000.00	0.143	0.00	0.55
$Li^+ - Mn^{3+}$	0.00	0.00	0.00	
$Li^+ - O^{2-}$	30000.00	0.154	0.00	
$Mn^{3+} - Mn^{3+}$	33883.92	0.156	16.00	1.65
$Mn^{3+} - O^{2-}$	18645.84	0.195	22.00	
$O^{2-} - O^{2-}$	11782.76	0.234	30.22	-1.1
Interaction	A (eV)	ρ(Å)	C (eV Å^6)	charge
$Ca^{2+} - Ca^{2+}$	10000.00	0.2300	0.00	1.2
$Ca^{2+} - Si^{2+}$	0.00	0.00	0.00	
$Ca^{2+} - O^{2-}$	131400.0	0.1875	60.00	
$Si^{4+} - Si^{4+}$	0.00	0.00	0.00	2.4
$Si^{4+} - O^{2-}$	18003.7572	0.2052	133.5381	
$O^{2-} - O^{2-}$	1388.773	0.36232	175.0	-1.2

The crystal structure of both compounds at the initial state is summarized in Table 2 and shown in Figure 1. The initial atomic coordinates were taken from [29]. Size effects of the simulated systems are expected to be small using properly large cells, and by applying periodic boundary conditions in all three dimensions. At first, the samples are relaxed at a temperature of around 300 K using an isothermal-isobaric (NPT) ensemble for 20 ps. After relaxation of the samples, the compounds are heated up to the target temperature of 2900 K for Ca_2SiO_4 and 2700 K for $LiMnO_2$. These high temperatures were chosen to ensure that all compounds are in liquid state. At the target temperature, the samples are relaxed again for 1000 ps. All visualizations as well as the analysis of the radial distribution function and the coordination analysis are done by the software tool OVITO-PRO [30].

Table 2. Compounds used in the simulations, their crystal systems, space groups, dimensions and the number of atoms.

Compound	Crystal System	Space Group	Volume (Å^3)	Number of Atoms
$LiMnO_2$	Orthorhombic	Pmmn	151165	16416
Ca_2SiO_4	Hexagonal	P6$_3$mc	202262	14112
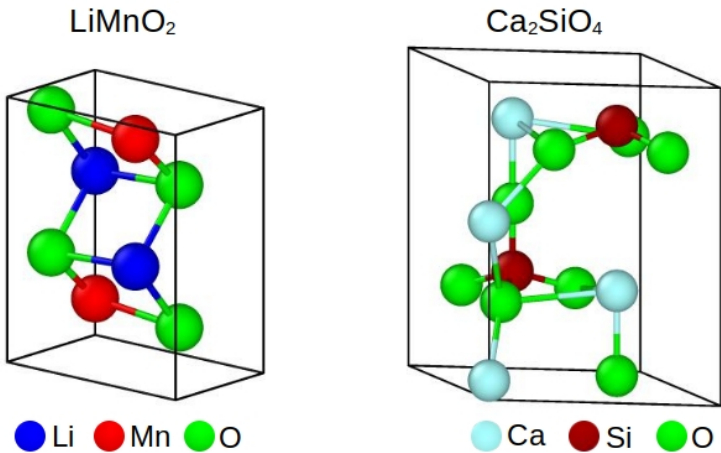
Figure 1. Left: structure of $LiMnO_2$ with Mn (red), Li (blue) and O (green). Right: Ca_2SiO_4 with Ca (light blue), Si (red) and O (green)

2.2. Calphad Model

The commercial databases FToxide and FactPS [13] were used for heterogeneous phase behavior and composition during equilibrium solidification. The system considered solid, liquid, and gaseous phases, while latter are assumed at fixed partial pressures, *e.g.*, oxygen at 0.21 bar. A Modified Quasichemical Model (MQM) was used for the liquid slag [31–33], where the manganese oxidation states Mn(II) and Mn(III) are considered [13]. Solid phase with stoichiometric compounds and solid solutions are also computed based on FToxide and FactPS [13].

2.3. Chemicals

Chemicals were obtained from different suppliers (BASF, Ludwigshafen, Germany; Carl Roth, Karlsruhe, Germany; CWS Chemiewerk Bad Köstritz, Bad Köstritz, Germany; Merck, Darmstadt, Germany) in per analysi grade or better (unless otherwise noted): Aluminium nitrate nona hydrate ($\geq$ 98 %), ammonia (25 wt%, technical), ammonium nitrate, calcium hydroxide, citric acid monohydrate, hydrogen peroxide (35 wt%), Köstrosol 0830AS (ammonia stabilized silicon oxide nanoparticles in water, 8 nm, 30 wt%), lithium hydroxide (98 %+), manganese(II) oxide, manganese(II/III) oxide, manganese(III) oxide, manganese(IV) oxide, manganese(II) nitrate tetra hydrate ($\geq$ 98 %), nitric acid (65 wt%), potassium bisulfate, and sulfuric acid (98 wt%), and were used for the slag preparation as well as in the synthesis of references. Dilutions were performed with ultra-pure water (> 18.2 MΩ cm, Purelab Flex 4, ELGA Veolia). Sodium tetra borate and hydrochloric acid (37 wt%) were used for fuse beads followed by leaching for ICP-OES analysis. Cellulose (micro crystalline, for optical measurements) and poly(imide) foil (Conrad electronic, Hirschau, Germany) were used for XANES pellet preparation.

Glaced porcellain crucibles (15 mL, wide form) were used from IDL for synthesis of the precursor. The crucibles were cleaned in boiling diluted piranha acid followed by boiling 10 % nitric acid and boiling ultra-pure water (each step for 2 h). At last a heating step 1273 K for 2 h was performed before usage. The final slag was prepared in platinum rhodium (90/10) crucibles. They were cleaned several times with a melt of potassium bisulfate followed by rinsing in 10 % nitric acid and ultra-pure water.

2.4. Instrumentation and Measurements

2.4.1. Oven

Sintering of the powders prepared by sol-gel-synthesis yielding the precursor was performed in a Nabertherm L 3/11 furnace with minimal air supply. Synthesis of the final slag was realised in a Nabertherm HT 40/17 high temperature furnace.

2.4.2. XANES

Lab X-ray absorption near edge structure analysis (lab-XANES) was done with an EasyXAFS easyXES100-extended [5,34,35]. The setup composes of a Pd/W X-ray tube (powered at 25 kV / 3 mA), a Si(110) spherically bent crystal analyzer and a Ketek ASAS-M1 silicon drift detector with a helium filled flight path between all components. Further informations about the setup are described in literature [5,34–36]. Evaluation was performed with custom Python scripts following the ATHENA package [37]. Energy calibration was done with a manganese foil (ExafsMaterials) according to Wittkowski *et al.* [5]. The energy range is set to 6482 – 6739 eV (ΔE = 0.25 eV, t = 2 s) and 6739 – 6899 eV (ΔE = 1 eV, t = 1 s) resulting in *approx.* 40 min per measurement. Each specimen is measured at least six times with the same number of I_0 measurements (80 mg pellet of pure cellulose).

The specimens were prepared as pellets (16 mm diameter) encapsulated in poly(imide) foil consisting of up to 20 mg of sample with 80 mg cellulose. References were chosen according to the possible presence in the slags and include manganese(II) oxide MnO, manganese(II/III) oxide Mn_3O_4 (hausmannite), manganese(III) oxide Mn_2O_3, manganese(IV) oxide MnO_2 as well as galaxite $MnAl_2O_4$, lithium manganate(III) $LiMnO_2$, lithium manganate(III/IV) $LiMn_2O_4$, and lithium manganate(IV)

Li_2MnO_3. Latter were prepared by sol gel combustion with the same procedure as for the slag or by the procedure described by Wittkowski *et al.* [5].

2.4.3. PXRD

Powder X-ray diffraction analysis (PXRD) was performed with a PANalytical X-Pert Pro diffractometer with Co Kα excitation (λ = 1.789 $\AA$, 40 kV, 40 mA) as backloading sample in Bragg-Brentano geometry. Identification of the phases was evaluated with the PDF-2 ICDD database [38]. Rietveld refinement was performed with the program package Fullprof [39].

2.4.4. EPMA

A Cameca SX^{FIVE} FE Field Emission was used for Electron probe micro analysis (EPMA) consisting of single crystals with elemental determination and back scattered electron detection. Wavelength dispersive quantification was performed for Na Kα, Mg Kα, Al Kα, Si Kα, Ca Kα, Mn Kα. Certified reference materials (PandH Developments and Astimex Standards) were used for calibration. Free standing thin sections of the corresponding samples were coated with a carbon layer before measurements at 15 kV at smallest beam size (100 – 600 nm, Schottky type [40]). Typical limits of detection (LOD) are determined for this sample system with 100 ppm for Ca Kα and Al Kα, 140 ppm for Mg Kα and Si α), 230 ppm for Na Kα, and 1150 ppm for Mn Kα. Visualisation of the rawdata was achieved by the peaksight-binary-parser within the HussariX package by Jokubauskas [41].

2.4.5. ICP-OES

Fuse beads were prepared by mixing 100 mg sample with 2.5 g sodium tetra borate and subsequent heating to 1323 K for 20 min. The beads were leached with diluted hydrochloric acid and filled to 200 mL final volume. The stock solutions were diluted 1:20 for ICP-OES measurement performed with an Agilent ICP-OES 5100 as well as a Varian Vista-MPX evaluating Li 670.78 nm, Al 396.15 nm, Ca 422.67 nm, Mg 279.55 nm, Mn 257.61 nm, Si 251.61 nm, and Pt 214.42 lines. Matrix adapted external calibration (10 μg·L^{-1} – 10 mg·L^{-1}) was done using blank preparations. Each sample was analysed in two replicates. The limits of detection (LOD) were determined considering three times the residual standard deviation devided by the slope of the calibration.

2.4.6. CHNS

Elemental analysis (CHNS) of the precursors was done with an Elementar varioMICRO CHNS with four replicates per sample (about 3 mg per run). Elemental analysis (CHNS) yielded 5.6 $\pm$ 0.2 wt% nitrogen as well as minor fractions of 0.5 $\pm$ 0.2 wt% hydrogen, and 0.19 $\pm$ 0.03 wt% carbon.

2.4.7. Micro-XRD, -XRF and XANES

Micro analysis on the thin sections was performed at the Diamond Light Source on end station I18 [42]. The beam was focused with Kirkpatrik-Baez mirrors to 2 $\times$ 2 μm spot size. Energy resolution is given with $\Delta E/E$ = 1.4 $\times 10^{-4}$ by a Si(110) double crystal monochromator. Data acquisition was performed with a Vortex-ME4 silicon drift detector (1 mm thickness) for XRF, an Excalibur area detector (115 $\times$ 100 mm active area) for XRD, and an ionisation chamber for the photon flux. Calibration of the XRD area detector was done with lanthanum boride LaB$_6$ powder sample while energy calibration for XANES is determined with a Mn foil (Goodfellow Cambridge). Reference spectra were measured using the same pellets from lab-XANES with 10 $\times$10 μm area scans for better statistics. Micro-XRF and micro-XRD were determined at 18 keV with a dwell time of 0.1 s per point. Micro-XANES in fluorescence mode was performed at Mn K-edge with the following energy regions: 6500 – 6538 eV (ΔE = 9.5 eV), 6540.25 eV, 6542 – 6557.5 eV (ΔE = 0.5 eV), and 6560 – 6800 eV (ΔE = 50 eV). For each energy 2D scans were obtained with a dwell time of 0.5 s per point. Linear combination fits of the normalized XANES spectra were done in the region 6538 – 6537 eV. Data evaluation included the usage of DAWN [43,44] for micro-XRF/XRD, MANTiS and TXM Wizard for micro-XANES [45,46], and PyFAI for micro-XRD processing and calibration [47,48].

2.5. Slag Analogue Preparation

Borosilicate beakers (1 L, high shape) and glaced porcelain crucibles were cleaned with 40 wt% sulfuric acid / 6 wt% hydrogen peroxide for 2 h at reflux, followed by 10 wt% nitric acid for 2 h at reflux, and ultra-pure water for 2 h at reflux. Between each cleaning step multiple rinsings with ultra-pure water were performed.

In an 1 L borosilicate beaker 0.323 g lithium hydroxide, 2.707 g calcium hydroxide, and 1.690 g manganese(II) nitrate tetra hydrate were dissolved in 50 mL 30 % nitric acid. Afterwards, 15.761 g citric acid mono hydrate were added under heating to reflux. At reflux the pH value was adjusted to about 6 with 25 % ammonia. Excess water was removed by boiling until the mixture thickens to a syrup followed by the addition of 3.1 mL Köstrosol 0830AS. With the heating plate set to maximum (723 K) the mixture was heated until self ignition set in. If the combustion wasn't fully obtained, about 5 g ammonium nitrate and 10 mL ultra-pure water were added to the cooled beaker followed by another ignition procedure. The total amount of substances was set to 75 mmol requiring two to three ignition steps compared to 25 mmol total amount of substances using only one combustion step [24]. The sol-gel combustion was prepared four times to result in 28.84 g powder. The powder was finely ground with 21.77 g ammonium nitrate before heating the mixture in three portions up to 753 K yielding 10.62 g of precursor.

The slag preparation was performed in duplicate with 3 g of precursor in platinum rhodium (90/10) crucibles up to a temperature of 1673 K. The heating program was adapted according to earlier studies [5,6,15] comprising of the following temperature steps: 298 K to 323 K (0.21 K·min^{-1}, 2.5 h holding time), 323 K to 993 K (2.8 K·min^{-1}), 993 K to 1573 K (2.3 K·min^{-1}, 2 h holding time), after cooling to ca. 1173 K (about 4.4 K·min^{-1}) a final heating to 1673 K was set (25 K·min^{-1}, 0.75 h holding time).

The liquid slags were extracted from the furnace at 1673 K and poured onto a steel plate resulting in a fast-cooling yielding 2.013 g (run A) and 2.135 g (run B) of the final slag, respectively. The beads were cut in two pieces with a) one half for free standing thin film preparation and b) the other half for further analysis which was ground in an agate ball mill to a fine powder. The thin films were prepared on glass substrate with an 3 mm hole for transmission measurements resulting in a free-standing thin film in that spot. In following this is described as fast-cooled slag. A thin film section of a slow-cooled slag with similar composition was directly used from Schnickmann *et al.* for microscopic characteristics (micro-XRF and micro-XANES) with its preparation and characterisation described earlier. [6].

3. Results and Discussion

3.1. Bulk Characteristics of the Solidified Li$_2$O-MnO$_x$-SiO$_2$-CaO

The oxide system studied here represents a simplified slag that may be obtained in Li-ion battery pyrometallurgical recycling. The major elements Ca and Si as well as Li are present. Manganese as potential EnAM forming element was added in an amount which should allow all the Li to be bound in a lithium manganate EnAM. Manganese is part of most novel Li-ion battery cathodes materials, accordingly its presence is expected in the slag. Aluminum, though it is used as current collector and housing material in batteries, was not considered in this synthetic slag to keep the system as simple as possible. Its presence leads to much larger number of compounds [6]. In an actual recycling process, it would be possible to separate housing and collectors prior to the pyrometallurgical procedure. The synthesis aim was to produce a solidified product including fast cooling having a composition of 2.4 wt% of Li$_2$O, 9.3 wt% Mn$_2$O$_3$, 37.2 wt% CaO and 13 wt% SiO$_2$. The bulk composition of the final product was verified by ICP-OES and yielded in general the expected amount, however somewhat less Li and Mn and more Si and Ca in two replicates (slag A and B, see Table 3). The comparison of the molar fractions (without carbon, oxygen, nitrogen, and hydrogen) gives information on actual losses *i.e.* lithium by about 10 % are found while the silicon, calcium, and manganese compositions

are unaltered (see Table 3). Trace elements present in the products were below the limits of detection (LOD) given for Mg (0.63 wt%), Al (0.21 wt%), and Pt (0.34 wt%).

Table 3. Initial and final concentration in wt% and mol% of elements in the synthesised slag analogue determined by ICP-OES. For the molar fractions only lithium, silicon, calcium, and manganese are considered.

| mass fraction / wt%	lithium	silicon	calcium	manganese
expected	2.4	13.0	37.2	9.3
precursor	1.7 ± 0.1	8.9 ± 0.4	26.3 ± 0.7	6.6 ± 0.6
final slag (run A)	2.1 ± 0.1	12.3 ± 0.4	34.9 ± 0.7	9.7 ± 0.6
final slag (run B)	2.0 ± 0.1	12.7 ± 0.4	36.0 ± 0.7	9.3 ± 0.6
molar fraction / mol%	lithium	silicon	calcium	manganese
expected	18.0	24.4	48.7	9.0
precursor	18.0 ± 1.5	23.8 ± 1.5	49.2 ± 2.6	9.0 ± 0.9
final slag (run A)	17.0 ± 1.1	24.5 ± 1.2	48.6 ± 1.9	9.8 ± 0.7
final slag (run B)	16.2 ± 1.1	24.9 ± 1.2	49.6 ± 1.9	9.3 ± 0.7

The oxidation state of Mn in the bulk material was obtained using lab-XANES [5]. The Mn K-edge shift of the synthesis precursor matches well Mn OS: +4 (see Li_2MnO_3 reference Figure 2). During the high temperature step the decomposition of Mn^{4+} to Mn^{3+} takes place, with the XANES spectra resembling the lithium manganate(III) $LiMnO_2$ with small variations due to the possible presence of Mn species with lower oxidation state, *e.g.*, hausmannite Mn_3O_4 or manganese(II) oxide MnO (Figure 2). The change of Mn oxidation state due to high temperatures seen here, was also described by Longo *et al.*, Paulsen and Dahn, as well as Schnickmann *et al.* [6,7,49].
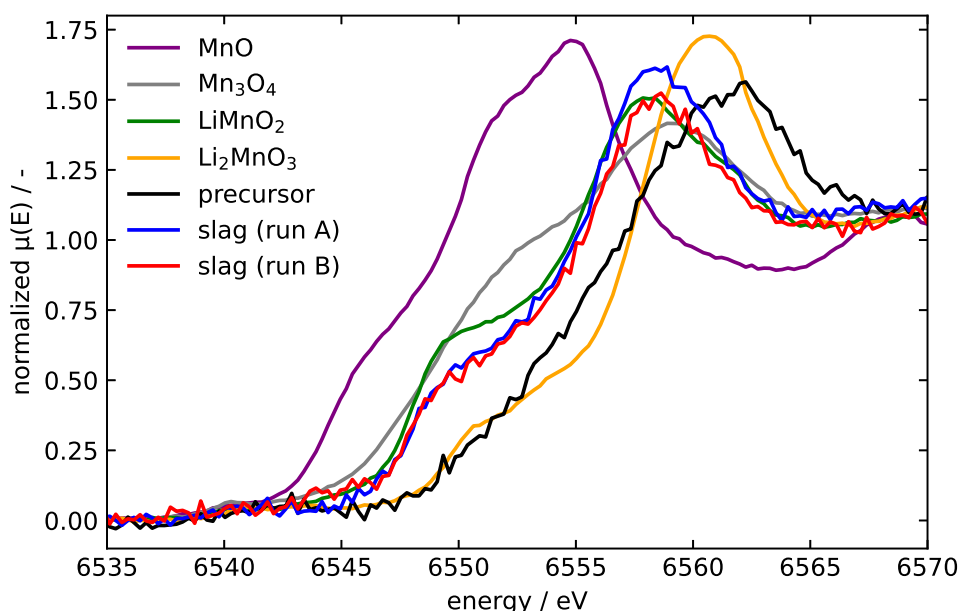
Figure 2. XANES spectra of the Mn K-edge of the slag analogue (precursor and final slags) and the reference compounds MnO, Mn_3O_4, $LiMnO_2$, and Li_2MnO_3.

The diffractograms were obtained from powder samples (laboratory PXRD) as well as from the sum of micro-XRD measurements of a free standing thin section of the sample. The PXRD of the bulk sample in Figure 3, panel A indicates the presence of β–Ca_2SiO_4 (larnite). Lithium manganate(III), $LiMnO_2$, as well as other possible lithium manganates could not be identified, unambiguously. Nevertheless, peaks are present in the bulk diffractogram which are not related to β–Ca_2SiO_4. Due to a high

background, based on severe fluorescence, as well as strong overlay because of the high number of peaks given by β–Ca_2SiO_4, these peaks could not be assigned to any compound, yet.
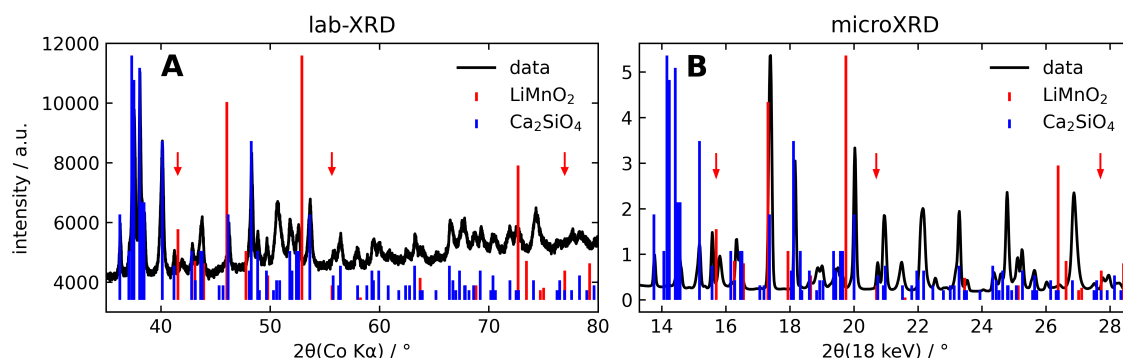
Figure 3. Laboratory powder XRD and summed micro-XRD from thin section for the quickly cooled melt (run A) with indicated references from PDF-2 database (Ca_2SiO_4 00-009-0351, $LiMnO_2$ 00-035-0749). Note that the micro-XRD diffractorgram exhibits lower backgrounds, which makes it easier to identify reflexes. The red arrows indicating the reflexes possibly associated with the Li-Mn-O compound.

Regarding the sum diffractogram of SR-micro-XRD (see Figure 3, panel B) it has to be mentioned, that the sample (free standing thin film) does not fulfill ideal powder conditions. Therefore, the intensity distribution of the respective reflexes cannot be taken into account and refinement according to the Rietveld method is not possible. Nevertheless, β–Ca_2SiO_4 can be clearly identified based on the respective reflex positions. Similar to the PXRD measurement, reflexes which do not belong to β–Ca_2SiO_4 occur, *e.g.* here at 15.8°, and which might be associated with an Li-Mn-O compound. Three of these reflexes are indicated by red arrows in Figure 3. These reflexes will be discussed further in the micro-XRD section.

The XANES spectra show a predominant presence of Mn OS: +3 species, which resembles $LiMnO_2$. The shoulder suggest the presence of a lithium manganate. The PXRD does not support the presence of crystalline $LiMnO_2$, but shows reflexes not explained by the larnite stemming from a Li-Mn-O compound or compounds.

3.2. Temperature Dependent Mn Species Evolution from Thermodynamics

Thermodynamic calculations can show the dependence of the Mn oxidation state from the gas phase oxygen concentration and the temperature.

Considering the bulk composition of: 5.11 wt% Li_2O, 14.88 wt% MnO_2, 52.09 wt% CaO, and 27.91 wt% SiO_2, the thermodynamic simulations were conducted under equilibrium conditions. In Figure 4 (left side), the release behavior of oxygen from the melt at high temperature is presented at a certain partial pressure of oxygen, 0.21 bar. Additionally, the valence of the manganese in the melt at lower temperatures, where solid phases already appear, is described in Figure 4 (right side). It is shown that the Mn OS: +3 amount decreases and at the same time the Mn OS: +2 amount increases by lowering the temperature. At 1673 K, 99.2 mol% of the manganese in the liquid slag is in Mn OS: +3. This indicates, that if the slag is cooled down fast from the temperature 1673 K, manganese is mainly in the Mn OS: +3 and the Mn OS: +2 is suppressed. This is also concluded by the experimental findings *i.e.* the XANES discussed before. The model allows to estimate the influence of temperature and oxygen gas phase concentration on the Mn oxidation state in equilibrium. The effect introduced by oxygen shuttle as described by Sasabe & Akamura and Nagata & Sasabe [9,50] and non-equilibrium processes can not be described at this time. The microscopic characteristics of the synthesized slag sample are discussed in the following sections. They also show mainly the presence of Mn OS: +3, where Mn OS: +2 was found in very few grains of Mn_3O_4 and with strong evidence in low concentrations in the Ca_2SiO_4 grains.
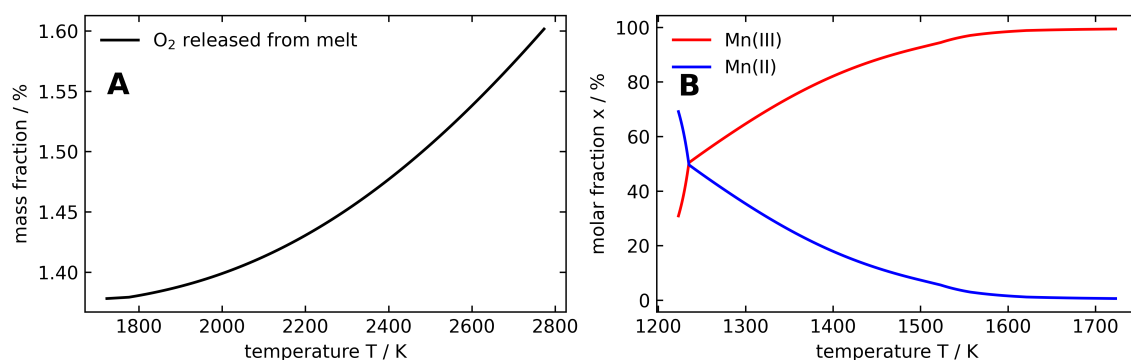
Figure 4. Left: Temperature dependent oxygen release from the melt at p(O$_2$) = 0.21 bar. Right: Temperature dependent manganese valence of the liquid slag at P(O$_2$) = 0.21 bar. The red line represents the Mn(III) in the liquid slag where the blue line shows the Mn(II).

3.2.1. Microscopic Characteristics

The results on the bulk chemistry indicates the presence of larnite and a Li-Mn^{3+}-oxide, with a composition similar to LiMnO$_2$. The microscopic observation of the slag reveals information on the spatial distribution, minor phases and possibly non-crystalline parts of the sample. The morphology of the grains and their inter-connectivity can be used as basis for a hypothesis of the genesis of the compounds. Using electron probe micro analysis (EPMA) the shape of the grains becomes visible. Here, large grains with smooth roundish curvature have formed, at their rims either channels of "residual melt" or grains with bright droplet, which seem to have separated from these grains are present. An example of a back scattering electron image (BSE) is displayed in Figure 5. The spot 1 is located in the large round grains, spot number 2 is located in the bright droplets and number three in the channels of the residual melt.
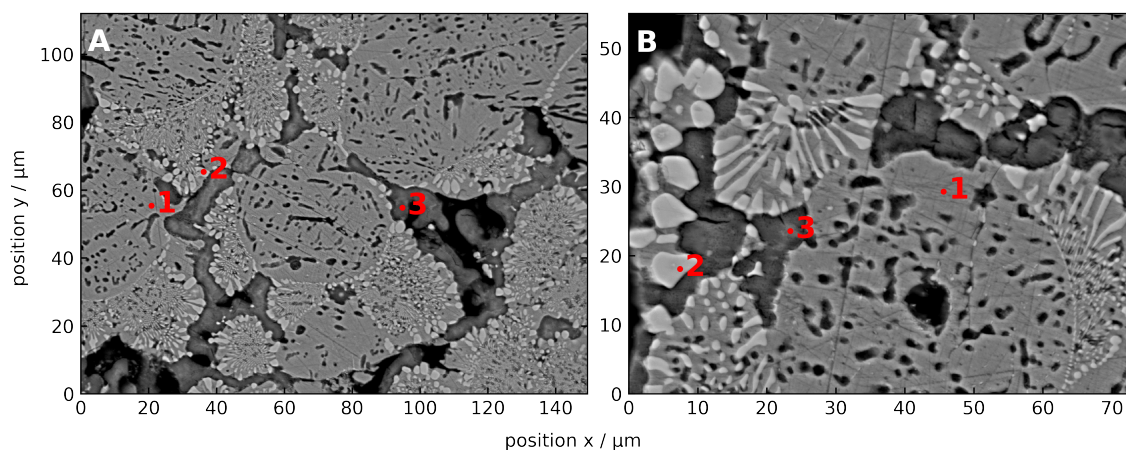
Figure 5. BSE images of the slag analogue. Three characteristic features can be distinguished overall the whole thin section and are annotated with red numbers: Phase 1 is located in large round shape grains of a uniform grey colour indicating a constant density; phase 2 is located in a bright droplet like feature. The brighter colour indicates a higher density compared to the other structures; finally phase 3 is located in a channel which is characterized by colours of darker grey indicating the presence of a lower density material.

With the characteristic X-ray emission the composition at the selected spots is determined. Using virtual component fitting the concentration of oxygen and lithium, which are not available from the experiment can be concluded [51]. The characteristic morphological features were studied quantitatively by several point measurements. The results for the large grain and the bright droplets are shown in Table 4. They suggest that the large grains (phase 1 in Figure 5) are largely Ca$_2$SiO$_4$ with minor amounts of Mn and the stoichiometric composition of (Ca$_{(2.00)}$Mn$^{2+}_{(0.02)}$)$_{2.02}$(Si$_{(0.99)}$)$_{0.99}$O$_4$

(n = 20). The bright droplets (phase 2 in Figure 5) contain most of the Mn and the composition is in agreement $LiMnO_2$ with the specific composition $(Li_{(1.86)}Mg_{(0.07)})Mn^{3+}_{2.00}O_4$ (n = 25). The residual melt (phase 3 in Figure 5) has a composition (n = 53) of 6.7 $\pm$ 0.7 wt% manganese, 34.6 $\pm$ 2.0 wt% calcium, 12.5 $\pm$ 0.8 wt% silicon, 0.42 $\pm$ 0.25 wt% magnesium, 0.12 $\pm$ 0.06 wt% aluminium, and 30.5 $\pm$ 1.1 wt% oxygen (total 85.2 $\pm$ 2.9 wt%). The virtual component fitting of the calcium-silicate phase predicts that Mn is present in the OS: +2 as a silicate. The elemental maps also obtained with the EPMA, show that Ca and Si are correlated, while Mn is mainly anti correlated with Ca and Si in agreement with the point measurements. The back-scatter images as well as the elemental maps of Mg, Mn, Ca and Si for two regions are displayed in Figure 6. The BSE image (Figure 5, panel B) is shown in the top row, while for the bottom row a new region was chosen to confirm the findings.
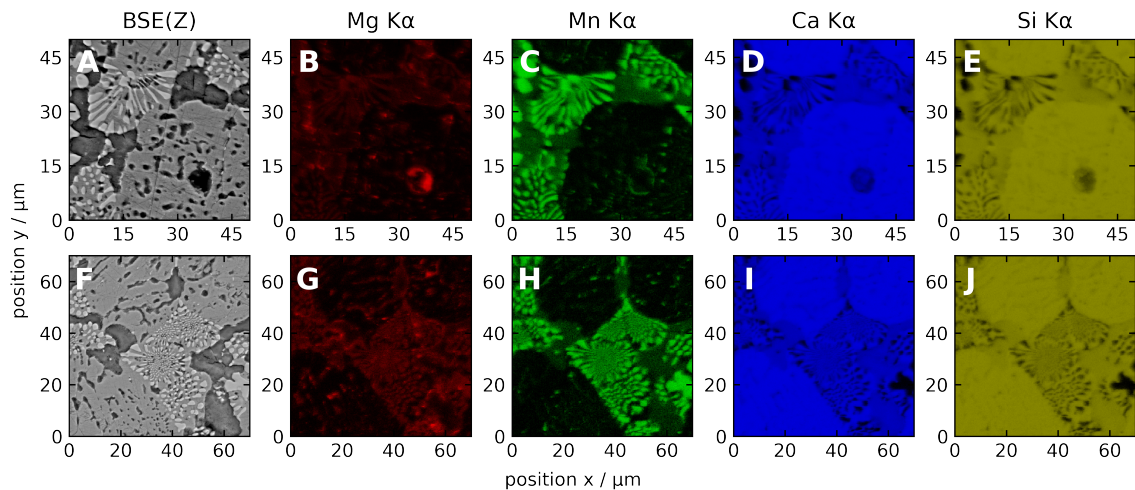

Figure 6. Mapping results obtained from EPMA exemplary from two regions of the specimen (top and bottom), A and F: BSE images, false color images: Mg Kα (B and G, red), Mn Kα (C and H, green); Ca Kα (D and I, blue), and Si Kα (E and J, yellow).

Table 4. Mean mass fractions of marked phases in Figure 5 with EPMA (WDXRF) and virtual components.

| mass fraction / wt% | phase 1: $(Ca_{(2.00)}Mn^{2+}_{(0.02)})_{2.02}(Si_{(0.99)})_{0.99}O_4$ | | | phase 2: $(Li_{(1.86)}Mg_{(0.07)})Mn^{3+}_{2.00}O_4$ | | |
	Ca_2SiO_4	Mn_2SiO_4	total	$LiMnO_2$	$MgMn_2O_4$	total
Li	–	–	–	6.83	–	6.83
Mn(II)	–	0.64	0.64	–	–	–
Mn(III)	–	–	–	54.03	4.13	58.16
Si	15.62	0.16	15.78	–	–	–
Ca	45.70	–	45.70	–	–	–
Mg	–	–	–	–	0.91	0.91
O	36.03	0.37	36.41	31.47	2.40	33.88
sum	97.35	1.17	98.52	92.33	7.45	99.78

The Mn oxidation states in the $LiMnO_2$ and the Ca_2SiO_4 predicted by the virtual component fitting was studied by species analysis using micro-XANES, with slightly lower spatial resolution at the Diamond Light Source at end station I18. A large area of the specimen was analysed by micro-XRF to identify the grains followed by energy scans to determine the Mn K-edge absorption edge fine structure at every pixel. The structure of the edges were compared with spectra obtained from Mn reference compounds. The XANES of manganese oxides spanning oxidation states from +2 to +4 including lithium manganates are displayed in Figure 7, panel A and B. As expected, the energy of the main edge shifts with higher oxidation state to higher energies. Additionally, the lithium bearing compounds show a low energy shoulder as a common characteristic. The references were used in linear combination fittings to identify the Mn species in each pixel. Three different mostly spatial separated Mn species were identified. These are a Li-Mn^{3+}-oxide, $Mn_3^{2.67+}O_4$ and an unidentified species. The main Mn species shows the shoulder characteristic for lithium manganates and a main

edge shift characteristic for Mn OS: +3. The $Mn_3^{2.67+}O_4$ seems to be associated with the Li-Mn^{3+}-oxide and the unidentified species is present in the Ca_2SiO_4. The XANES of the three regions is shown in Figure 7 C.
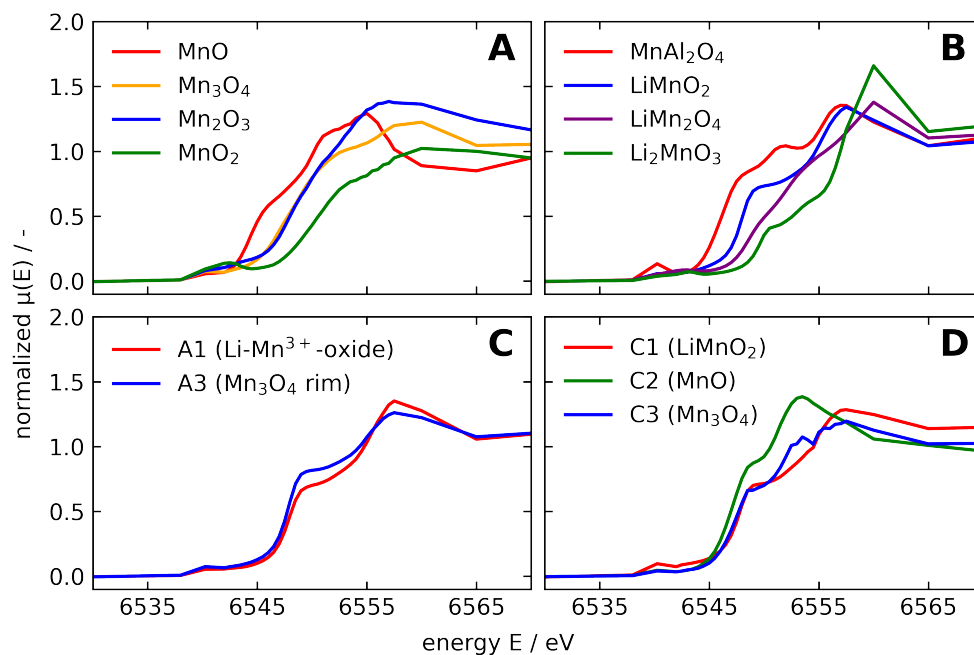
**Figure 7.** Manganese K-edge XANES spectra of manganese specimens. A: Manganese oxides references $Mn^{2+}O$ (red), $Mn_2^{3+}O_3$ (blue), $Mn_3^{2.67+}O_4$ (yellow) and $Mn^{4+}O_2$ (green). B: Lithium manganese oxides $LiMn_2^{3.5+}O_4$ (purple), $Li_2Mn^{4+}O_3$ (green), $LiMn^{3+}O_2$ (blue) and manganese aluminium oxide $Mn^{2+}Al_2O_4$ (red). C: Two species identified in the fast-cooled slag specimen with ROI 1 Li-Mn^{3+}-oxide (red) and ROI 3 $Mn_3^{2.67+}O_4$ rim (blue). D: Three species identified in the slowly-cooled slag specimen with ROI 1 Li-Mn^{3+}-oxide (red), ROI 2 Mn^{2+} species (green) and ROI 3 $Mn_3^{2.67+}O_4$ (blue).

The speciation of Mn in the Ca_2SiO_4 is not possible due to a) overlapping with the Li-Mn^{3+}-oxide spectra from greater depths (the free-standing thin film is polished to about 50 μm thickness and only small grains of the Li-Mn-O compounds in depth will dominate the XANES), b) lower concentrations expressed as edge-jump (up to 10 times lower than in the red areas), and c) resulting errors in the linear combination fit (LCF) expressed as R factor. The R factor describes the goodness-of-fit with perfect results at R = 0 and rising with increasing errors [52]. The same applies for the Mn_3O_4 rim, while here better statistics and changes in the edge region towards the reference spectrum allow a correct assignment. The micro-XANES LCF high fit errors correlate with low concentrations (*e.g.*, in the Ca_2SiO_4 grains). The correlation is visualized in Figure S1 in the supplementaries.

In Figure 8 an overview of the elemental distribution is shown as RGB image in the part A with Ca (blue), Mn (red) and Pt < 0.34 wt% (green). The low concentrated contamination of Pt stemming from the crucibles is included as it is enriched in the residual melt. The species distribution is displayed from a close up which is indicated as a white box. The elemental distribution of the close up area is shown in Figure 8 B and the assigned Mn species in the part C. The Mn species obtained from the micro-XANES data are Li-Mn^{3+}-oxide (red), Mn species unknown (green) and $Mn_3^{2.67+}O_4$ (blue).
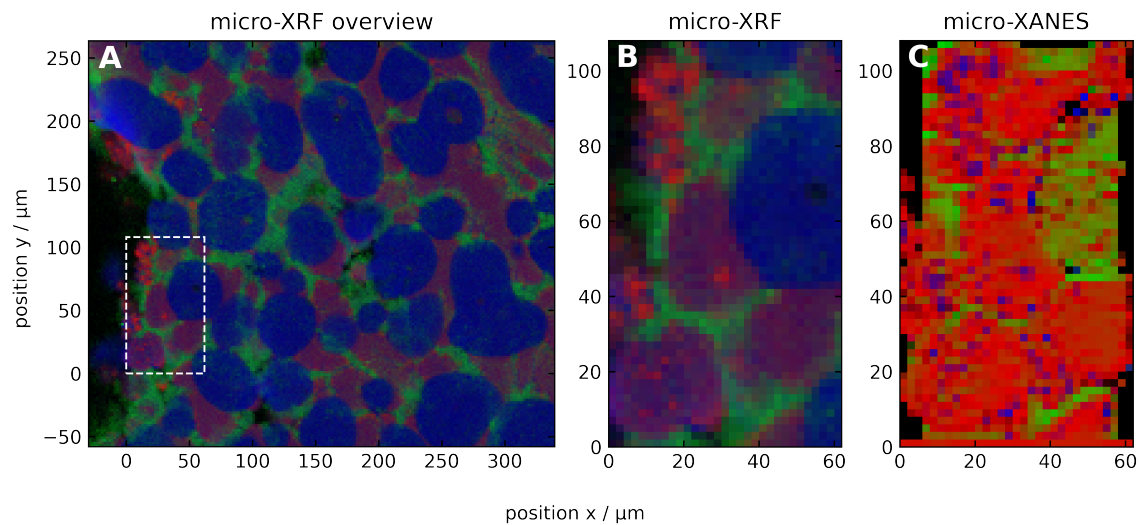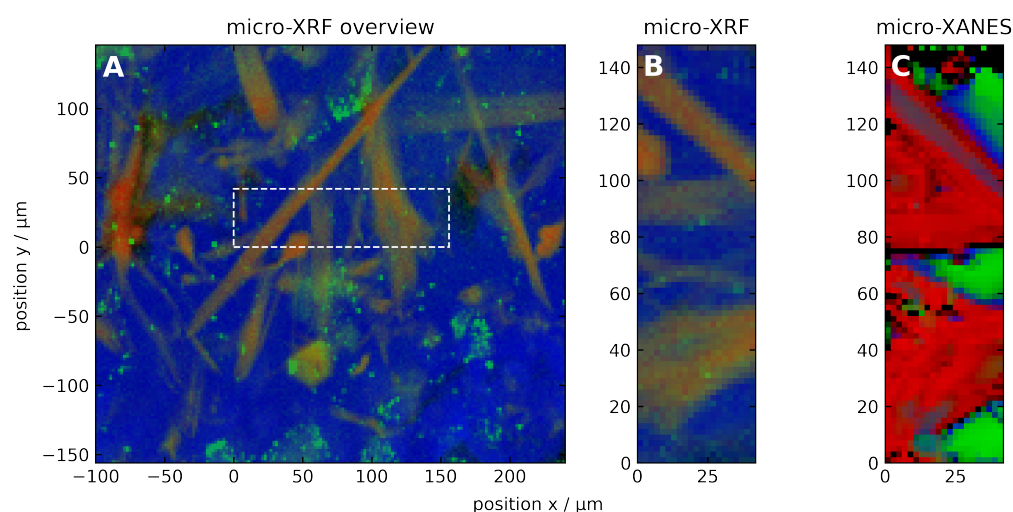
Figure 8. RGB false color image of the fast-cooled slag analogue A overview with the selected area indicated and B close up of the elemental distribution of Ca (blue), Mn (red) and Pt < 0.34 wt% (green), C distribution of the Mn species obtained from the micro-XANES data: Li-Mn^{3+}-oxide (red), Mn species unknown (green) and Mn$_3^{2.67+}$O$_4$ (blue).

The bulk PXRD was inconclusive on the presence of LiMnO$_2$. The EPMA with virtual components as well as the micro-XANES indicate the presence of a compound/compounds with a composition similar to LiMnO$_2$. In Figure 3 the summed diffractogram of micro-XRD measurements showed reflexes which do not belong to β–Ca$_2$SiO$_4$ (2θ(18 keV) = 15.8°, 20.6°, and 27.5°) and which could possibly belong to a Li-Mn-O structure. Processing of the micro-XRD data allows to test for spatial correlation of these reflexes with the Mn-rich grains. The intensity map for the reflex 15.8° 2θ is shown in Figure 9 (the reflex 15.8° 2θ matched this position, while the 27.5° reflex showed the same map with lower intensity). In panel A the intensity map for the reflex is shown resembles a structure around the large grains. In panel B the micro-XRF data for Ca and Mn are shown, exhibiting no clear correlation with the above mentioned intensity map (Figure 9, panel A). Panel C, Figure 9, on the other hand, shows transmission data, capturing the grain structure in depth. Transmission data as well as the micro-XRD data was obtained through the entire thin section giving evidence that several grains were present within the thickness of the thin section. The overlay with the reflex data of 2θ = 15.8° show that it represents a structure surrounding larnite grains. The "droplet spray" structure visible in the EPMA incorporates most of the Mn present in the sample (Figure 9, panel B), therefore the intensities plotted in panel C indicate the presence of an Li-Mn-O structure around the larnite grains. The exact structure of this Li-Mn-O compound cannot be identified, unambiguously, which is basically given by the severe overlay with larnite intensities. The EPMA images show, that the Li-Mn-O grains are mostly quite small with 2-5 μm, the isolation of LiMnO$_2$ from larnite reflexes with an resolution of 2 μm in combination with the several grain layers in the 50 μm thick specimen was not possible. Regarding the calculated stoichiometry of the Li-Mn-O compound, LiMnO$_2$ would be a promising candidate, additionally, the (011) peak of LiMnO$_2$ fits to the certain 2θ position shown in Figure 9, panel A. Nevertheless, prior PXRD measurements could not confirm the presence of the structure of LiMnO$_2$. Therefore, LiMnO$_2$ is either present in the sample in very small quantities, which can only be visualized by micro-XRD analysis or the observed intensities belong to another structurally different Li-Mn-O compound.
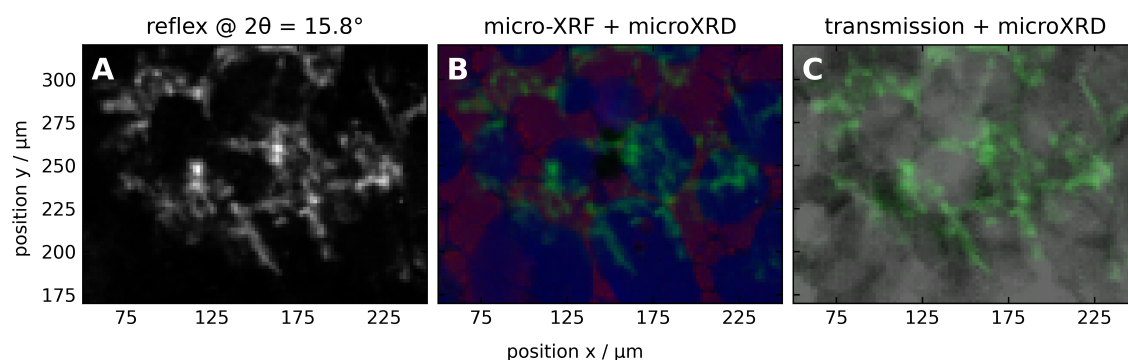
Figure 9. A: Micro-XRD intensity map of possible LiMnO$_2$ (011) reflex at 15.8° 2θ. B: RGB false color image of micro-XRD map of 15.8° reflex (green) and micro-XRF elemental distribution of Ca (blue) and Mn (red). C: False color image of micro-XRD map of 15.8° reflex (green) and transmission signal (grey scale).

In conclusion the Mn oxidation state in the Mn rich grains determined from the micro-XANES is +3 and matches well the results from the EPMA. The Mn$_3^{2.67+}$O$_4$ phase was not identified initially with the EPMA but with the micro-XANES. The Mn oxidation state in the larnite could not be determined. In a slowly cooled slag with similar composition, which has been described previously [6] LiMnO$_2$ and larnite were identified. The larnite also contained low amounts of Mn. Here, the slowly-cooled slag was also subjected to micro-XANES, to confirm the Mn species and attempt the speciation of Mn in the larnite. The Mn OS: +3 was confirmed in the Mn rich needles and like in the fast cooled counterpart, hausmannite was identified in adjacent areas. Due to the better statistic of the measurements it was possible to identify the Mn species being +2. Deeper insights on the chemical composition of the compound were not obtained. The XANES spectra of the reference oxides were not matching. In future studies manganese silicates, *e.g.*, tephroite Mn$_2$SiO$_4$, could be an interesting reference. In the Figure 7 the Mn K-edge XANES spectra for the three identified species are displayed. These are LiMn^{3+}O$_2$ (ROI 1 red), Mn$_3^{2.67+}$O$_4$ (ROI 3 blue) and the Mn +2 (ROI 2 green). The distribution of elements and Mn species are shown in Figure 10. In A an RGB false color image of the elemental distribution is shown with the Ca matrix in blue, Mn in red and Pt in green (Pt is present in very low concentrations from the crucible). In part C the Mn species distribution is shown. The Mn rich needle like grains match with LiMn^{3+}O$_2$ (red). At the rims of the needle the spectra match Mn$_3^{2.67+}$O$_4$ (blue) and in the calcium matrix the Mn+2 species is present (green).

Figure 10. RGB false color image of the slowly-cooled slag analogue A overview with the selected area indicated and B close up of the elemental distribution of Ca (blue), Mn (red) and Pt < 0.34 wt% (green), C distribution of the Mn species obtained from the micro-XANES data: LiMn^{3+}O$_2$ (red), Mn +2 species (green) and Mn$_3^{2.67+}$O$_4$ (blue).

*3.3. Modelling of Mn Species Evolution and of Potential Melt Structures*

A central question in the genesis of compounds in the slag is which parameters govern the oxidation state of redox-active species, here manganese. We have shown that Mn of OS: +3 is the main species in the slags studied here and there is strong evidence that Mn of OS: +2 is present in the calcium silicate phase. The oxidizing agent responsible for higher valence is most likely oxygen, which needs to be transferred between the gas phase and the melt. Parameters influencing the oxygen transfer, are its concentration in the gas phase, the temperature dependent equilibrium, the viscosity of the melt [2,8] and the concentration of labile redox active metal ions in the melt [9]. In general a lower viscosity favours a higher permeability of oxygen [1,2,8]. The viscosity of different composited slags can be estimated by considering network breaking, *i.e.* Fe and Mn ions, and network-forming ions, *e.g.* Si, as well as calculating the degree of polymerization Q [1,2]. However, the local viscosity will be influenced by phase separation and is usually not addressed in these models. Liquid-liquid separation as well as liquid-solid separation can commonly occur in silicate based melts. If a immiscibility gap is thermodynamically present manifest itself at low viscosities. Permeation of gas phase oxygen has been intensively studied with respect to redox-active oxide like Fe and Mn, it was found that increasing concentration of these significantly increase oxygen permeability because of a redox-mediated dissolution of oxygen [9,50]. As these ions also act as network breakers both effects, lowering of viscosity and facilitating the redox-mediated oxygen transport occur together with the presence of manganese ions.

3.3.1. Potential Local Melt Structures and Viscosity by MD Simulations

Assuming the phases $LiMn^{3+}O_2$ and Ca_2SiO_4 were present in micro-areas of the melt, those were chosen to simulate their MD at high temperatures. Starting from the mean square displacement function of the ions at different temperatures the diffusion coefficients of the individual ions in the two phases are calculated. It was previously shown that Li^+ ions are most mobile [24], this was found here as well in the lithium manganate phase with *e.g.* diffusion coefficients of 0.45×10^{-9} m²·s⁻¹ at 1700 K and 20.28×10^{-9} m²·s⁻¹ at 2100 K. The manganese cations and the oxygen anions have quite similar diffusion coefficients with 0.7×10^{-11} m²·s⁻¹ for Mn^{3+} and 0.3×10^{-11} m²·s⁻¹ for O^{2-} at 1700 K as well as 3.77×10^{-9} m²·s⁻¹ for Mn^{3+} and 4.99×10^{-9} m²·s⁻¹ for O^{2-} at 2100 K (Figure 11 left). In the calcium silicate phase the mobility of the ions is significantly lower. The Ca^{2+} ions are most mobile (however much less compared to lithium ions) in this phase and reach a diffusion coefficient of 5.94×10^{-9} m²·s⁻¹ at 2400 K. The silicon and oxygen ions have similar mobility lower than the one of the calcium ions of 2.26×10^{-9} m²·s⁻¹ Si^{4+} and 2.77×10^{-9} m²·s⁻¹ O^{2-} at 2400 K (Figure 11 right).

Mean coordination number of ions can be computed by counting the number of neighbors of an ion within a given cutoff distance and averaged over ions of the same species. It is found that each Si ion moves in the slag is surrounded by 4 oxygen ions. The coordination numbers for Si-Si interactions are a good indicator for the degree of polymerization. The average coordination number given from the distribution in Figure 12 is 1.05 showing only small polymerization degree for Si-Si interaction. For Si-O interactions the mean coordination number is close to 4 representing the formation of SiO_4 tetrahedra shown in Figure 12 (right side).

The affinity for Si-O bonds can be best shown from the radial distribution function (RDF) at melt conditions (see Figure S2, supplementary). Figure S2 visualises the RDF for $LiMnO_2$ and Ca_2SiO_4 at 2100 K and 2400 K, respectively. For Ca_2SiO_4 the strong Si-O bonds are well visible with Ca being incorporated into the SiO_x network. For the Li-Mn-O interactions in $LiMnO_2$ comparable bond lengths for Li-O and Mn-O were obtained. Consequently, the viscosity of the calcium silicate phase is significantly higher compared to the lithium manganate phase. At 1800 K, a temperature close to the melt temperature during slag preparation (1673 K) the viscosity of the $LiMn^{3+}O_2$ is 50.51 mPa·s while the viscosity of the Ca_2SiO_4 is higher > 634.74 mPa·s (Figure 13).
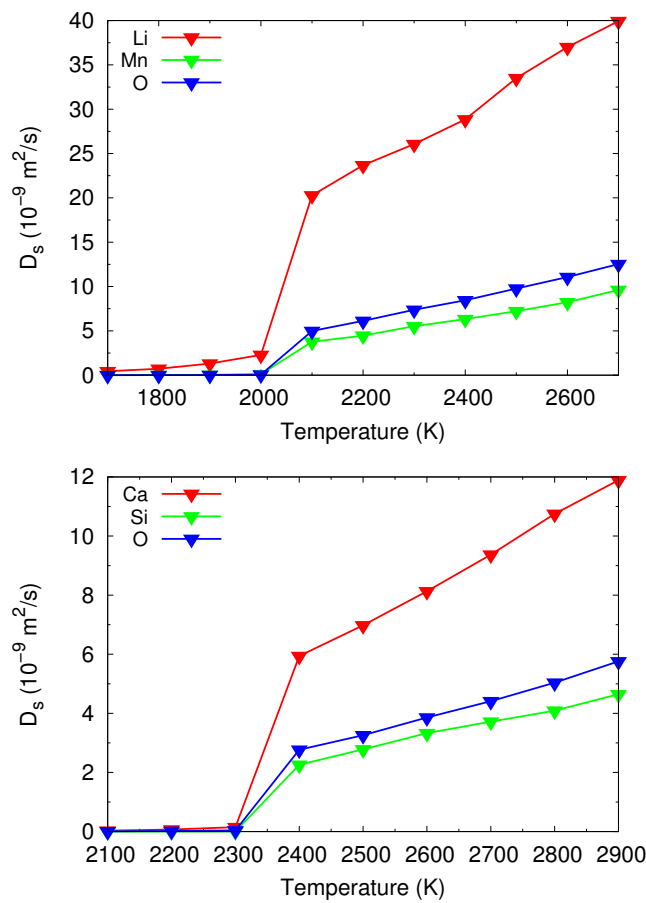
Figure 11. Temperature dependent diffusion coefficient for the different ions. Left: Li$^+$ (red), Mn^{3+} (green) and O^{2-} (blue). Right: Ca^{2+} (red), Si^{4+} (green) and O^{2-} (blue).
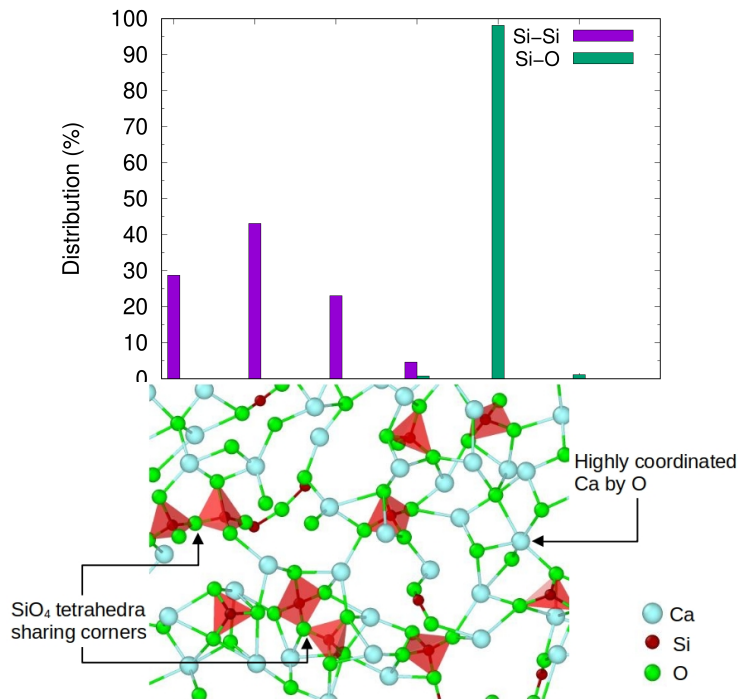
Figure 12. Distribution of coordination numbers of Si-Si and Si-O interactions (left). Graphic representation of the Ca$_2$SiO$_4$ slag structure (right).
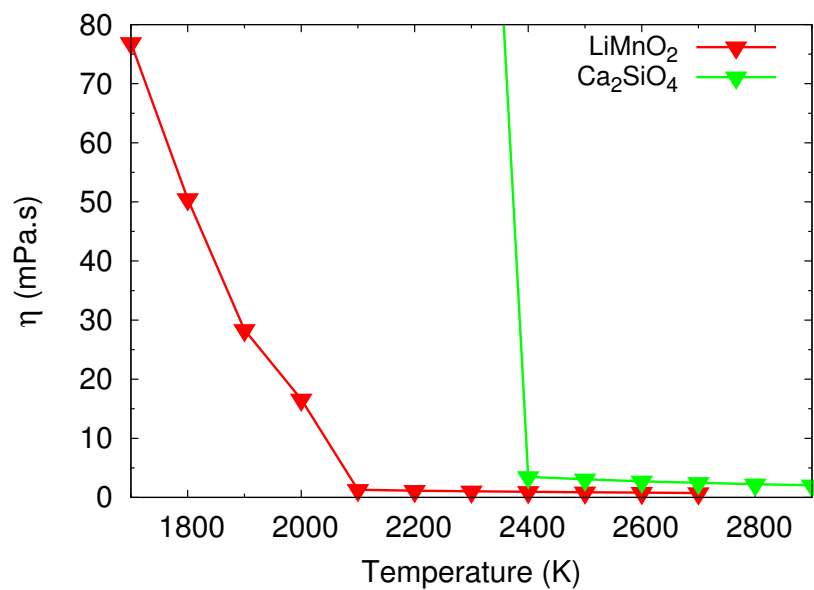
Figure 13. Temperature dependent viscosity of $LiMn^{3+}O_2$ (red) and Ca_2SiO_4 (green).

The elemental analysis (cf. to section 3.1) and the EPMA has shown that the phases are not pure. The calcium silicate contains *approx.* 0.7 wt% Mn and the lithium manganate(III) phase contains 0.9 wt% magnesium. Accordingly, it is expected that the actual viscosity of the phases are lower than those simulated. The contamination will be included in future simulations.

4. Conclusions

Tailoring pyro-metallurgical Li-ion battery recycling slags with the goal to direct the solidification to scavenger compounds for critical elements, requires an understanding on the evolution of manganese oxidation state. Manganese at this time will be present in these system because of its valuable role in Li-ion cathode materials [49] and because its affinity to oxygen will most of the time rather enter the slag phase than the metal phase in the pyro-metallurgical process. Depending on its oxidation state and the presence of other metal ions Mn can either be present in a single compound, found in the Ca-Si-Li-Mn-Mg-O system or in spinel solid solution with a broad distribution of concentration *e.g.* in the Ca-Si-Li-Mn-Mg-Al-O system [6]. However, only a single compound is favorable for recovery. The manganese compounds identified in that study were also rich in lithium and the Mn species suggested by EPMA were either only Mn OS: +3 or both Mn OS: +2 and OS: +3 were present. According to thermodynamic considerations an even higher Mn oxidation state could result in a lithium rich single compound Li_2MnO_3 [49]. Therefore, it is important to understand what governs the Mn oxidation state evolution. Here the formation of Mn oxidation state in a calcium silicate system containing *approx.* 17 wt% lithium manganate(III) was studied. The solidified product, which has encountered steep cooling rates, showed separation into round large larnite grains and small Li-Mn-Oxide droplets close to each other (spray-like pattern). Mainly Mn OS: +3 was formed in the Li-Mn-rich grains with evidence the chemical composition being $LiMnO_2$. Manganese OS: +2 was found in small concentration in the calcium silicate phase and in a hausmannite phase. Thermodynamic simulations under the assumption that the melt is homogeneous predicts a dominance of Mn^{3+} over Mn^{2+} with a fraction of 99 mol% at experimental temperature of 1673 K. The fast cooling may have preserved this status. The viscosity of a Ca_2SiO_4 and $LiMnO_2$ as potential micro compositions of the melt at 1700 K obtained with MD simulation showed significant differences. The viscosity of the $LiMnO_2$ phase was indeed lower than the one of the Ca_2SiO_4, which could suggest that lower viscosity will support higher Mn oxidation state, at least up to a certain temperature. In future studies it is necessary to better understand phase separations occurring in the melt and adapt the compositions for the simulations accordingly. Experimentally, the interplay of the oxygen gas phase concentration, the temperature

and various melt compositions (viscosities) need to be studied, including the potential influence of elements qualifying for an oxygen shuttle transport.

Conflicts of Interest: The authors declare no conflict of interest. The funders had no role in the design of the study, in the collection, analyses, or interpretation of data, in the writing of the manuscript, or in the decision to publish the results.

References

1. Mills, K.C. The Influence of Structure on the Physico-chemical Properties of Slags. *ISIJ International* **1993**, *33*, 148–155. doi:10.2355/isijinternational.33.148.

2. Mills, K.C.; Hayashi, M.; Wang, L.; Watanabe, T. Chapter 2.2 - The Structure and Properties of Silicate Slags. In *Treatise on Process Metallurgy*; Seetharaman, S., Ed.; Elsevier: Boston, 2014; pp. 149–286. doi:https://doi.org/10.1016/B978-0-08-096986-2.00008-4.

3. Elwert, T.; Strauss, K.; Schirmer, T.; Goldmann, D. Phase composition of high lithium slags from the recycling of lithium ion batteries. *World Metall. -Erzmetall* **2012**, *65*, 163–171.

4. Acker, S.; Namyslo, J.C.; Rudolph, M.; Strube, F.; Fittschen, U.E.A.; Qiu, H.; Goldmann, D.; Schmidt, A. Polyether-tethered imidazole-2-thiones, imidazole-2-selenones and imidazolium salts as collectors for the flotation of lithium aluminate and spodumene. *RSC Adv.* **2023**, *13*, 6593–6605. doi:10.1039/D2RA07627F.

5. Wittkowski, A.; Schirmer, T.; Qiu, H.; Goldmann, D.; Fittschen, U.E.A. Speciation of Manganese in a Synthetic Recycling Slag Relevant for Lithium Recycling from Lithium-Ion Batteries. *Metals* **2021**, *11*, 188. doi:10.3390/met11020188.

6. Schnickmann, A.; Hampel, S.; Schirmer, T.; Fittschen, U.E.A. Formation of Lithium-Manganates in a Complex Slag System Consisting of Li2O-MgO-Al2O3-SiO2-CaO-MnO—A First Survey. *Metals* **2023**, *13*. doi:10.3390/met13122006.

7. Longo, R.C.; Kong, F.T.; KC, S.; Park, M.S.; Yoon, J.; Yeon, D.H.; Park, J.H.; Doo, S.G.; Cho, K. Phase stability of Li–Mn–O oxides as cathode materials for Li-ion batteries: insights from ab initio calculations. *Phys. Chem. Chem. Phys.* **2014**, *16*, 11233–11242. doi:10.1039/C4CP00937A.

8. Jahanshahi, S.; Sun, S.; Zhang, L. Effects of transition metals on physicochemical properties of slags. 2007, pp. 1–20.

9. Nagata, K.; Sasabe, M. Permeability Coefficient of Oxygen in Molten Slags and Its Mechanisms. *ISIJ International* **2020**.

10. Lukas, H.; Fries, S.G.; Sundman, B. *Computational Thermodynamics: The Calphad Method*; Cambridge University Press, 2007. doi:10.1017/CBO9780511804137.

11.   Li, H.; Qiu, H.; Schirmer, T.; Goldmann, D.; Fischlschweiger, M. Tailoring Lithium Aluminate Phases Based on Thermodynamics for an Increased Recycling Efficiency of Li-Ion Batteries. *ACS ES&T Engineering* **2022**, *2*, 1883–1895, [https://doi.org/10.1021/acsestengg.2c00105]. doi:10.1021/acsestengg.2c00105.

12.   Li, H.; Ranneberg, M.; Fischlschweiger, M. High-Temperature Phase Behavior of Li2O-MnO with a Focus on the Liquid-to-Solid Transition. *JOM* **2023**.

13.   Bale, C.; Bélisle, E.; Chartrand, P.; Decterov, S.; Eriksson, G.; Gheribi, A.; Hack, K.; Jung, I.H.; Kang, Y.B.; Melançon, J.; Pelton, A.; Petersen, S.; Robelin, C.; Sangster, J.; Spencer, P.; Van Ende, M.A. FactSage thermochemical software and databases, 2010–2016. *Calphad* **2016**, *54*, 35–53. https://doi.org/https://doi.org/10.1016/j.calphad.2016.05.002.

14.   Chakrabarty, S.; Li, H.; Fischlschweiger, M. Calphad-informed thermodynamic non-equilibrium simulation of non-isothermal solid-state reactions of magnesium aluminate spinel based on the thermodynamic extremal principle. *Materialia* **2023**, *28*, 101723. doi:https://doi.org/10.1016/j.mtla.2023.101723.

15.   Schirmer, T.; Qiu, H.; Li, H.; Goldmann, D.; Fischlschweiger, M. Li-Distribution in Compounds of the Li2O-MgO-Al2O3-SiO2-CaO System—A First Survey. *Metals* **2020**, *10*, 1633. doi:10.3390/met10121633.

16.   Sommerfeld, M.; Vonderstein, C.; Dertmann, C.; Klimko, J.; Oráč, D.; Miškufová, A.; Havlík, T.; Friedrich, B. A Combined Pyro- and Hydrometallurgical Approach to Recycle Pyrolyzed Lithium-Ion Battery Black Mass Part 1: Production of Lithium Concentrates in an Electric Arc Furnace. *Metals* **2020**, *10*, 1069. doi:10.3390/met10081069.

17.   Zhou, C.; Li, J.; Wang, S.; Zhao, J.; Ai, L.; Chen, Q.; Chen, Q.; Zhao, D. Development of Molecular Dynamics and Research Progress in the Study of Slag. *Materials* **2023**, *16*. doi:10.3390/ma16155373.

18.   Kim, Y.; Park, H. Estimation of TiO2-FeO-Na2O slag viscosity through molecular dynamics simulations for an energy efficient ilmenite smelting process. *Scientific Reports* **2019**, *9*, 17338. doi:10.1038/s41598-019-53961-1.

19.   Ma, S.; Li, K.; Zhang, J.; Jiang, C.; Bi, Z.; Sun, M.; Wang, Z. Effect of MnO content on slag structure and properties under different basicity conditions: A molecular dynamics study. *Journal of Molecular Liquids* **2021**, *336*, 116304. doi:https://doi.org/10.1016/j.molliq.2021.116304.

20.   Liang, D.; Yan, Z.; Lv, X.; Zhang, J.; Bai, C. Transition of Blast Furnace Slag from Silicate-Based to Aluminate-Based: Structure Evolution by Molecular Dynamics Simulation and Raman Spectroscopy. *Metallurgical and Materials Transactions B* **2017**, *48*, 573–581. doi:https://doi.org/10.1007/s11663-016-0855-y.

21.   Zhang, X.; Liu, C.; Jiang, M. Molecular Dynamics Simulations of Melt Structure Properties of CaO–Al2O3–Na2O Slag. *Metallurgical and Materials Transactions B* **2021**, *52*, 2604–2611. doi:10.1007/s11663-021-02184-9.

22.   Deng, L.; Zhang, X.; Zhang, M.; Jia, X. Effect of CaF2 on viscosity, structure and properties of CaO-Al2O3-MgO-SiO2 slag glass ceramics. *Journal of Non-Crystalline Solids* **2018**, *500*, 310–316. https://doi.org/https://doi.org/10.1016/j.jnoncrysol.2018.08.018.

23.   Chen, Y.; Pan, W.; Jia, B.; Wang, Q.; Zhang, X.; Wang, Q.; He, S. Effects of the amphoteric behavior of Al2O3 on the structure and properties of CaO–SiO2–Al2O3 melts by molecular dynamics. *Journal of Non-Crystalline Solids* **2021**, *552*, 120435. doi:https://doi.org/10.1016/j.jnoncrysol.2020.120435.

24.   Hampel, S.; Alhafez, I.A.; Schirmer, T.; Merkert, N.; Wunderlich, S.; Schnickmann, A.; Li, H.; Fischlschweiger, M.; Fittschen, U.E.A. Engineering Compounds for the Recovery of Critical Elements from Slags: Melt Characteristics of Li 5 AlO 4 , LiAlO 2 , and LiAl 5 O 8. *ACS Omega* **2024**. https://doi.org/10.1021/acsomega.4c00723.

25.   Fittschen, U.E.; Hampel, S.; Schirmer, T.; Merkert, N. Multimodal spectroscopy and Molecular Dynamic simulations to understand redox-chemistry and compound formation in pyrometallurgical slags: example of manganese oxidation state with respect to lithium recycling. *Applied Spectroscopy Reviews LAPS* **2024**. doi:https://doi.org/10.1080/05704928.2024.2350988.

26.   Thompson, A.P.; Aktulga, H.M.; Berger, R.; Bolintineanu, D.S.; Brown, W.M.; Crozier, P.S.; in 't Veld, P.J.; Kohlmeyer, A.; Moore, S.G.; Nguyen, T.D.; Shan, R.; Stevens, M.J.; Tranchida, J.; Trott, C.; Plimpton, S.J. LAMMPS - a flexible simulation tool for particle-based materials modeling at the atomic, meso, and continuum scales. *Comp. Phys. Comm.* **2022**, *271*, 108171. doi:10.1016/j.cpc.2021.108171.

27.   Cormack, A.; Du, J. Molecular dynamics simulations of soda–lime–silicate glasses. *Journal of Non-Crystalline Solids* **2001**, *293-295*, 283–289. 8th Int. Conf. on Non-Crystalline Materials, https://doi.org/https://doi.org/10.1016/S0022-3093(01)00831-6.

28. Sayle, T.X.T.; Ngoepe, P.E.; Sayle, D.C. Simulating Mechanical Deformation in Nanomaterials with Application for Energy Storage in Nanoporous Architectures. *ACS Nano* **2009**, *3*, 3308–3314. https://doi.org/10.1021/nn9009592.

29. Jain, A.; Ong, S.P.; Hautier, G.; Chen, W.; Richards, W.D.; Dacek, S.; Cholia, S.; Gunter, D.; Skinner, D.; Ceder, G.; Persson, K.A. Commentary: The Materials Project: A materials genome approach to accelerating materials innovation. *APL Materials* **2013**, *1*, 011002, [https://pubs.aip.org/aip/apm/article-pdf/doi/10.1063/1.4812323/13163869/011002_1_online.pdf]. doi:10.1063/1.4812323.

30. Stukowski, A. Visualization and analysis of atomistic simulation data with OVITO–the Open Visualization Tool. *Modelling and Simulation in Materials Science and Engineering* **2010**, *18*, 015012. doi:10.1088/0965-0393/18/1/015012.

31. Pelton, A.D.; Degterov, S.A.; Eriksson, G.; Robelin, C.; Dessureault, Y. The modified quasichemical model I—Binary solutions. *Metallurgical and Materials Transactions B* **2000**, *31*, 651–659. doi:10.1007/s11663-000-0103-2.

32. Pelton, A.D.; Chartrand, P. The modified quasi-chemical model: Part II. Multicomponent solutions. *Metallurgical and Materials Transactions A* **2001**, *32*, 1355–1360. doi:10.1007/s11661-001-0226-3.

33. Pelton, A.D. A general "geometric" thermodynamic model for multicomponent solutions. *Calphad* **2001**, *25*, 319–328. doi:10.1016/S0364-5916(01)00052-9.

34. Seidler, G.T.; Mortensen, D.R.; Remesnik, A.J.; Pacold, J.I.; Ball, N.A.; Barry, N.; Styczinski, M.; Hoidn, O.R. A laboratory-based hard x-ray monochromator for high-resolution x-ray emission spectroscopy and x-ray absorption near edge structure measurements. *Review of Scientific Instruments* **2014**, *85*, 113906. doi:10.1063/1.4901599.

35. Jahrman, E.P.; Holden, W.M.; Ditter, A.S.; Mortensen, D.R.; Seidler, G.T.; Fister, T.T.; Kozimor, S.A.; Piper, L.F.J.; Rana, J.; Hyatt, N.C.; Stennett, M.C. An improved laboratory-based x-ray absorption fine structure and x-ray emission spectrometer for analytical applications in materials chemistry research. *Review of Scientific Instruments* **2019**, *90*, 024106. doi:10.1063/1.5049383.

36. Lutz, C.; Fittschen, U.E.A. Laboratory XANES to study vanadium species in vanadium redox flow batteries. *Powder Diffraction* **2020**, pp. 1–5. doi:10.1017/S0885715620000226.

37. Ravel, B.; Newville, M. ATHENA, ARTEMIS, HEPHAESTUS: data analysis for X-ray absorption spectroscopy using IFEFFIT. *J. Synchrotron Radiat.* **2005**, *12*, 537–541. doi:10.1107/S0909049505012719.

38. Gates-Rector, S.; Blanton, T. The Powder Diffraction File: a quality materials characterization database. *Powder Diffraction* **2019**, *34*, 352–360. doi:10.1017/S0885715619000812.

39. Rodríguez-Carvajal, J. Recent advances in magnetic structure determination by neutron powder diffraction. *Physica B: Condensed Matter* **1993**, *192*, 55–69. doi:https://doi.org/10.1016/0921-4526(93)90108-I.

40. Jercinovic, M.J.; Williams, M.L.; Allaz, J.; Donovan, J.J. Trace analysis in EPMA. *IOP Conference Series: Materials Science and Engineering* **2012**, *32*, 012012. doi:10.1088/1757-899X/32/1/012012.

41. Jokubauskas, P. HussariX. https://github.com/sem-geologist/HussariX, 2024. [Online; accessed 16.01.2024].

42. Mosselmans, J.F.W.; Quinn, P.D.; Dent, A.J.; Cavill, S.A.; Moreno, S.D.; Peach, A.; Leicester, P.J.; Keylock, S.J.; Gregory, S.R.; Atkinson, K.D.; Rosell, J.R. I18–the microfocus spectroscopy beamline at the Diamond Light Source. *Journal of Synchrotron Radiation* **2009**, *16*, 818–824. doi:10.1107/S0909049509032282.

43. Basham, M.; Filik, J.; Wharmby, M.T.; Chang, P.C.Y.; El Kassaby, B.; Gerring, M.; Aishima, J.; Levik, K.; Pulford, B.C.A.; Sikharulidze, I.; Sneddon, D.; Webber, M.; Dhesi, S.S.; Maccherozzi, F.; Svensson, O.; Brockhauser, S.; Náray, G.; Ashton, A.W. Data Analysis WorkbeNch (DAWN). *Journal of Synchrotron Radiation* **2015**, *22*, 853–858. doi:10.1107/S1600577515002283.

44. Filik, J.; Ashton, A.W.; Chang, P.C.Y.; Chater, P.A.; Day, S.J.; Drakopoulos, M.; Gerring, M.W.; Hart, M.L.; Magdysyuk, O.V.; Michalik, S.; Smith, A.; Tang, C.C.; Terrill, N.J.; Wharmby, M.T.; Wilhelm, H. Processing two-dimensional X-ray diffraction and small-angle scattering data in DAWN 2. *Journal of applied crystallography* **2017**, *50*, 959–966. doi:10.1107/S1600576717004708.

45. Lerotic, M.; Mak, R.; Wirick, S.; Meirer, F.; Jacobsen, C. MANTiS: a program for the analysis of X-ray spectromicroscopy data. *Journal of Synchrotron Radiation* **2014**, *21*, 1206–1212. doi:10.1107/S1600577514013964.

46. Liu, Y.; Meirer, F.; Williams, P.A.; Wang, J.; Andrews, J.C.; Pianetta, P. TXM-Wizard: a program for advanced data collection and evaluation in full-field transmission X-ray microscopy. *Journal of Synchrotron Radiation* **2012**, *19*, 281–287. doi:10.1107/S0909049511049144.

47. Kieffer, J.; Karkoulis, D. PyFAI, a versatile library for azimuthal regrouping. *Journal of Physics: Conference Series* **2013**, *425*, 202012. doi:10.1088/1742-6596/425/20/202012.

48. Kieffer, J.; Wright, J.P. PyFAI: a Python library for high performance azimuthal integration on GPU. *Powder Diffraction* **2013**, *28*, S339–S350. doi:10.1017/S0885715613000924.

49. Paulsen, J.M.; Dahn, J.R. Phase Diagram of Li−Mn−O Spinel in Air. *Chemistry of Materials* **1999**, *11*, 3065–3079. doi:10.1021/cm9900960.

50. Sasabe, M.; Asamura, A. Transport phenomenon of oxygen through molten slags. *2nd International Symposium on Metallurgical Slags and Fluxes, 1984 (2nd Int Symp Metall Slags Fluxes 1984)* **1984**, pp. 651–667.

51. Schirmer, T. STOICHIOMETRIC CALCULATION OF LITHIUM-CONTAINING PHASES BASED ON SPATIALLY RESOLVED X-RAY ANALYSIS AND VIRTUAL COMPOUNDS. *Advances in X-Ray Analysis* **2022**, *65*, 45–56.

52. Gaur, A.; Shrivastava, B.D. Speciation using X-ray absorption fine structure (XAFS). *Review Journal of Chemistry* **2015**, *5*, 361–398. doi:10.1134/S2079978015040032.